



# Modelling aluminium nitride's refractive indices under various situations for optical simulations: a mixed research

Zaky A. Zaky<sup>1,2,3</sup> · M. Al-Dossari<sup>4</sup> · Mahmoud A. M. Hussien<sup>5</sup> · V. D. Zhaketov<sup>3,6</sup> · Arafa H. Aly<sup>1,7</sup>

Received: 17 July 2024 / Accepted: 8 September 2024 / Published online: 9 October 2024  
© The Author(s), under exclusive licence to Springer Science+Business Media, LLC, part of Springer Nature 2024

## Abstract

Recently, optical simulation has attracted more attention in different thin film applications. Each layer's thickness and refractive index are the most essential simulation parameters. This paper discusses and fits the refractive index of aluminum nitride at different geometrical and physical conditions over a wide wavelength range for optical simulations. This study simplifies the use of aluminum nitride in thin film-simulated applications and devices. Plotted curves and fitted equations with MATLAB scripts for aluminum nitride refractive indices at different conditions will be provided to minimize modeling errors.

**Keywords** Aluminum nitride · Refractive index · Fitting · Optical modeling · Substrate temperature

## 1 Introduction

Optical properties of a particular material are known as the changes that light experiences while interacting with it. The optical properties are impacted by the macroscopic and microscopic attributes of the material, including its surface properties and electronic structure. The way a material affects light is typically easier to detect than investigating its

---

✉ Zaky A. Zaky  
zaky.a.zaky@science.bsu.edu.eg

<sup>1</sup> TH-PPM Group, Physics Department, Faculty of Sciences, Beni-Suef University, Beni-Suef 62514, Egypt

<sup>2</sup> Academy of Scientific Research and Technology (ASRT), Cairo, Egypt

<sup>3</sup> Frank Laboratory of Neutron Physics, Joint Institute for Nuclear Research, Dubna, Russia 141980

<sup>4</sup> Department of Physics, Faculty of Science, King Khalid University, 62529 Abha, Saudi Arabia

<sup>5</sup> Physics Department, Faculty of Science, Assiut University, Assiut 71516, Egypt

<sup>6</sup> Moscow Institute of Physics and Technology (State University), Dolgoprudny, Moscow Oblast, Russia

<sup>7</sup> Department of Technical Sciences, Western Caspian University, 1001, Baku, Azerbaijan

macroscopic and microscopic characteristics in a direct way. Therefore, the optical properties of a material are frequently utilized to investigate its other features. Reflection, refraction, transmission, and absorption are the most well-known optical properties. One fundamental optical property that holds great significance is the refractive index (RI), associated with many of these optical properties (Kasap and Capper 2017).

The quotient of the velocity of light ( $c$ ) in space to its velocity ( $v$ ) in the medium is defined as the RI of an optical or dielectric medium, denoted as  $n=c/v$ . The formula for calculating the RI of a material is  $n = \sqrt{\epsilon_r \mu_r}$ , where  $\epsilon_r$  and  $\mu_r$  are the relative permittivity and the relative magnetic permeability, respectively, based on Maxwell's equations.  $\mu_r$  equals 1 in materials that are not magnetic. So, the result is  $n = \sqrt{\epsilon_r}$ . This relationship is highly beneficial in establishing a connection between a material's dielectric characteristics and its optical behavior at a specific frequency of concern. The dependence of RI on the light wavelength is described as dispersion. Also, as an electromagnetic wave (EM) propagates through a real medium, it not only disperses but also undergoes attenuation. This results in the wave losing energy through various mechanisms such as phonon generation (lattice waves), photogeneration, free-carrier absorption, and scattering. Within these substances, RI is a complex formula. The relationship between the complex RI ( $\hat{n}$ ), consisting of the real part ( $n$ ) and the imaginary part ( $k$ ), is  $\hat{n} = n - iK$  (Kasap and Capper 2017).

Investigating the optical properties, especially the RI, of aluminum nitride (AlN) thin films is of great interest due to their massive number of applications in electronics (Dogheche et al. 1999; Interrante et al. 1989). AlN, an III–V semiconductor compound (Gerlich et al. 1986) that crystallizes in the hexagonal wurtzite and cubic zincblende structure (Carlone et al. 1984), has exceptional optical characteristics such as considerable energy bandgap ( $\sim 5.9$ – $6.2$  eV), high RI, low-absorption coefficient of less than  $10^{-3}$ , large exciton binding energy, and significant dielectric properties (Choudhary et al., 2013; Xiong et al. 2012; Baek et al. 2007). This, in turn, made it a perfect fit for various optical and electronic uses, resulting in extensive research on it (Strite and Morkoç 1992; Morkoc et al. 1994; Davis 1991; Wang et al. 2005). Moreover, thin-layer AlN is recognized as a highly potential material for piezoelectric (Sinha et al. 2009; Gräupner et al. 1992) or electro-optic (Xiong et al. 2012; Huang et al. 2012) applications. These characteristics are closely linked to the crystal quality of the layer. The RI of AlN films was determined using the prism-coupling method, which can quickly assess and contrast films produced through processes like sputtering or epitaxy (Stolz et al. 2013). The significant association between microstructural and optical characteristics suggests that this optical approach can be used as a quick, non-destructive metal measuring instrument (Stolz et al. 2013).

AlN films/coatings can be grown using various techniques, including metal–organic chemical vapor deposition (MOCVD) using  $(CH_3)_3Al$  with  $NH_3$  (Zetterling et al. 1997; Rensch and Eichhorn 1985), ion beam sputtering (Chen et al. 2006), vacuum arc/cathodic arc deposition (Takikawa et al. 2001), reactive molecular beam epitaxy (Schupp et al. 2010), DC/RF reactive sputtering (Cheng et al. 2003; Venkataraj et al. 2006; Mahmood et al. 2003), pulsed laser deposition (Vispute et al. 1995), ion implantation (Ohira and Iwaki 1987), evaporation of Al with  $N_2$  (Yoshida et al. 1975), porous aluminum template (Wu et al. 2004), extended vapor–liquid–solid growth technique (Wu et al. 2003).

AlN materials have been created in various sizes and forms for functional applications, such as particles (Liu et al. 2009a, 2009b), whiskers (Drum and Mitchell 1964; Radwan and Bahgat 2007), plates (Rosenberg et al. 1991), nanowires (Wu et al. 2004), and three-dimensional (3D) porous structures (Shi et al. 2013; Boey and Tok 2003). 3D interconnected porous ceramic materials, specifically open-cell ceramic foams, are

extensively utilized as high-level functional materials in various vital applications like battery electrodes, heat exchangers, sensors, filters, and battery separators. Similarly, porous AlN is anticipated to offer a similar wide range of uses as it can supply a larger surface area and increased permeability compared to its solid form (Nam et al. 2018).

AlN thin films, a versatile ceramic material, have received significant interest for their prospective applications in telecommunications (computers, laptops, inverters, and TV remotes) (Chaurasia et al. 2019), microelectronics (Yu et al. 1992), biomedicine (Ou et al. 2006), micro-electro-mechanical systems (MEMS) (Kumar et al. 2019), piezoelectric applications such as ultrasonic transducers (Valbin and Sevely 2001), sensory applications (Yarar et al. 2016), bulk resonators (Zou et al. 2022), actuators (Sinha et al. 2009), bandpass filters (Zha et al. 2024), and energy harvesters (He et al. 2018). AlN can be stabilized with sapphire (Watanabe et al. 2008; Lu et al. 2018), GaN (Pezzagna et al. 2008), 6H-SiC (Watanabe et al. 2008), Si (Ababneh et al. 2020), SiO<sub>2</sub> (Bui et al. 2014), TiN (Goldsmith et al. 2017), Au (Goldsmith et al. 2017), glass (Venkataraj et al. 2006), graphite (Venkataraj et al. 2006), quartz (Venkataraj et al. 2006), microscopic slides (Venkataraj et al. 2006), etc.

Recently, the simulation of optical applications such as sensors (Zaky et al. 2022a, 2022b, 2023a, 2023b), smart windows (Zaky and Aly 2022), and solar cells (Luque-Raigón et al. 2019; Zhang et al. 2012) attracted more attention. The RI and thickness of each layer are the most essential simulation parameters. Zaky et al. (Zaky et al. 2024) used the fitted equations of DPV polymer as a sensitive material for gamma radiation to design a gamma dosimeter. Besides, the fitted equations of RIs for GaN (Zaky et al. 2023c, 2021a), Si (Zaky et al. 2021b), SiO<sub>2</sub> (Zaky et al. 2022c), seawater (Zaky and Aly 2021), and Ta<sub>2</sub>O<sub>5</sub> (Zaky et al. 2022d) were used in sensing applications.

Many experimental studies measure RIs in the form of figures without fitting the results in equations. Watanabe et al. (2008) measured the RIs of GaN and AlN, plotted the results, and wrote the Sellmeier general equation without mentioning the fitting parameters. Bui et al. (Bui et al. 2014) plotted the measured results without fitted equations. Despite the RI of AlN is very sensitive to small thicknesses lower than 40 nm, Ashrafi et al. (Ashrafi and Mohanty 2024) used a RI of thick AlN (2 mm) in their thin layer simulations (5 nm). As a result, it is crucial to discuss the effect of different parameters on the RI of AlN and simulate the measured results in fitted equations. So, fitting the RIs of AlN at different physical and geometrical conditions is a critical study.

Sellmeier equation is an empirical formula for the RI as a function of wavelength for a particular transparent medium (Gooch 2011). This empirical formula is used to determine the light dispersion of a specific medium. The general formula is  $n^2 = A + \sum_i \frac{B_i \lambda^2}{\lambda^2 - C_i^2}$ ,

where  $A$ ,  $B_i$  and  $C_i$  are constants. The wavelength ( $\lambda$ ) should be inserted in  $\mu\text{m}$ . Sellmeier formula is extremely helpful. It characterizes fairly accurately the RI over a wide wavelength range. Sellmeier coefficients are available for many materials in different databases. It is essential to indicate the validity range of the wavelength of any Sellmeier data.

The work studies RIs of AlN in different conditions. This material has a wide range of applications in optical and electronic devices, and studying its properties is an urgent task. The paper introduces new equations for calculating the RI of AlN, which makes it a significant contribution to modelling materials' optical properties. The RIs of AlN will be fitted at different thicknesses, measuring temperatures, wavelengths, sputtering setups, sputtering times, grown temperatures, back pressures, substrate temperatures, polarization states, gas flow ratios (Argon/Nitrogen), and RF sputtering power.

## 2 Basic equations, fitting, and discussion

The RIs of hexagonal AlN were measured with thicknesses of 9.23  $\mu\text{m}$  (measured by SEM with error less than 2%) by (Watanabe et al. 2009) at a wide range of temperatures of (24  $^{\circ}\text{C}$ , 253  $^{\circ}\text{C}$ , and 515  $^{\circ}\text{C}$ ) by spectroscopic ellipsometry across the wavelength from 0.27 to 0.80  $\mu\text{m}$  ( $\lambda$  in  $\mu\text{m}$ ). AlN films were grown by HVPE (hydride vapor phase epitaxy) on (0001)-oriented 6H-SiC substrates. The Sellmeir formula can be used to match the experimental data as follows:

At 24  $^{\circ}\text{C}$ :

$$n^2 = -1.431398 + \frac{4.615607\lambda^2}{\lambda^2 - 0.075320^2} + \frac{0.874942\lambda^2}{\lambda^2 - 0.180058^2}, \tag{1}$$

At 253  $^{\circ}\text{C}$ :

$$n^2 = -1.491258 + \frac{5.061819\lambda^2}{\lambda^2 - 0.087518^2} + \frac{0.504196\lambda^2}{\lambda^2 - 0.191831^2}, \tag{2}$$

At 515  $^{\circ}\text{C}$ :

$$n^2 = -1.342212 + \frac{4.876504\lambda^2}{\lambda^2 - 0.088099^2} + \frac{0.579228\lambda^2}{\lambda^2 - 0.192323^2} \tag{3}$$

As clear in Fig. 1, the RI of AlN increases by increasing the temperature, and gradually decreases with wavelength. Watanabe et al. (Watanabe et al. 2009) experimentally measured the thermo-optic coefficients ( $\frac{\partial n}{\partial T}$  in  $\text{K}^{-1}$ ) of AlN for wide range of temperatures from 24  $^{\circ}\text{C}$  to 515  $^{\circ}\text{C}$ . They fitted the thermo-optic coefficient across the wavelength range of 0.270–1.000  $\mu\text{m}$  ( $\lambda$  in  $\mu\text{m}$ ) as follows (Fig. 2):

$$\frac{\partial n}{\partial T} = 3.486 \times 10^{-6} \lambda^{-3} - 1.689 \times 10^{-5} \lambda^{-2} + 3.245 \times 10^{-5} \lambda^{-1} + 8.361 \times 10^{-6} \tag{4}$$

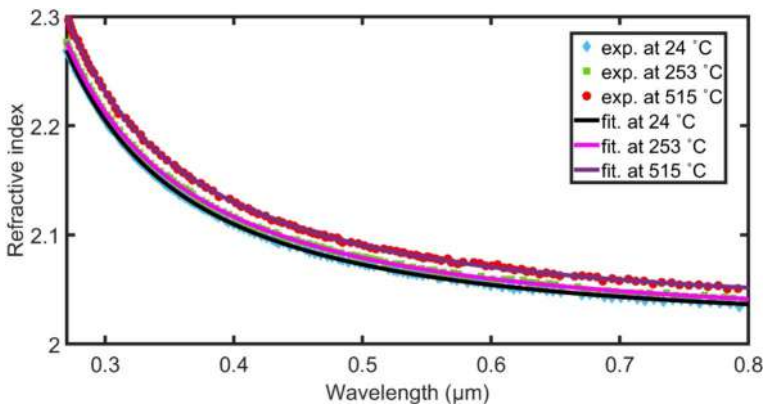


**Fig. 1** Experimental (Watanabe et al. 2008) and fitted RI (using Eqs. 1, 2, and 3) of AlN versus the wavelength at different temperatures (24  $^{\circ}\text{C}$ , 253  $^{\circ}\text{C}$ , and 515  $^{\circ}\text{C}$ )

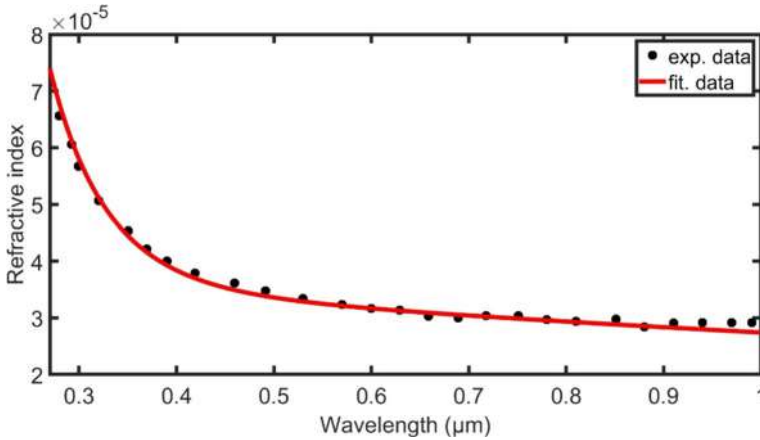


**Fig. 2** Experimental and fitted thermo-optic coefficient (using Eq. 4 and 5) (Watanabe et al. 2008) of AlN versus the wavelength at a wide range of temperatures from 24 °C to 515 °C

$$n(T) = n_{24^{\circ}C} + \frac{\partial n}{\partial T}(T - 24). \tag{5}$$

Figure 3 shows the indices of refraction of AlN with a thickness of 9.23 μm at wavelengths of 0.22 μm, 0.25 μm, 0.30 μm, and 0.50 μm. Up to 500 °C, the fitted index of refraction of AlN linearly increases with temperature and is recorded to coincide nicely with experimental data for wavelengths higher than the bandgap area. The correspondence between fitted results and experimental data decreases near the bandgap area (below 230 nm).

Bowman et al. (2018) measured 1 mm thick ordinary ( $n_o$ ) and extraordinary ( $n_e$ ) RI of AlN from wavelength of 0.46–1.90 μm at 25 °C using internal reflection from a calibrated rutile prism. They noticed that  $n_o$  is smaller than  $n_e$ , and both of them decrease gradually with

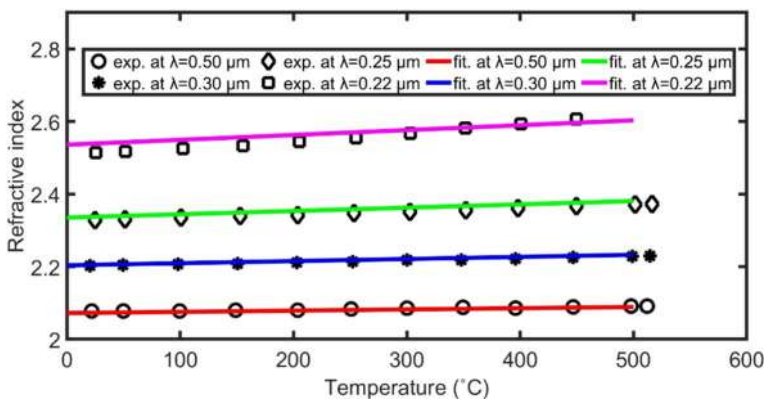


**Fig. 3** Experimental and fitted RI (using Eqs. 4 and 5) (Watanabe et al. 2008) of AlN versus the temperature at a wide range of wavelengths from 0.22 to 0.50 μm

wavelength. At lower wavelengths, both  $n_o$  and  $n_e$  strongly decrease, but they slightly decrease at longer wavelengths. By fitting the experimental results, we get a matched Sellmeir formula as follows (Fig. 4):

For ordinary AIN:

$$n_o^2 = -1.25870 + \frac{5.41928\lambda^2}{\lambda^2 - 0.10592^2} + \frac{5.67461\lambda^2}{\lambda^2 - 18.95342^2}. \tag{6}$$

For extraordinary AIN:

$$n_e^2 = 3.30853 + \frac{1.03812\lambda^2}{\lambda^2 - 0.23650^2} + \frac{8.13660\lambda^2}{\lambda^2 - 20.29733^2}. \tag{7}$$

In 2020, Ababneh et al. (2020) deposited and optically characterized AIN thin films on a silicon substrate at different sputtering setups. The thickness of samples changes from 125 to 1100 nm. As clear in Fig. 5, the RIs of samples S1, S2, S3, and S4 gradually decrease with increasing the wavelength from 0.25  $\mu\text{m}$  to 1.20  $\mu\text{m}$ . On the other hand, the RIs of samples S1, S2, S3, and S4 change with changing the sputtering setups of the sample preparation. By increasing the sputtering pressure, the oxygen contamination ratio increases, the incorporation of impurities increases, and RI decreases. By fitting the experimental results, we get a matched Sellmeir formula as follows (Fig. 5):

S1: At power of 1000 W, pressure of 0.2 Pa, 100%  $N_2$ , sputtering time of 1500 s, and thickness of 560 nm:

$$n^2 = -13.34087 + \frac{17.66188\lambda^2}{\lambda^2 - 0.06821^2} + \frac{67517\lambda^2}{\lambda^2 - 13287^2} \tag{8}$$

S2: At power of 500 W, pressure of 0.2 Pa, 100%  $N_2$ , sputtering time of 3000 s, and thickness of 540 nm:

$$n^2 = -12.01961 + \frac{16.30088\lambda^2}{\lambda^2 - 0.06943^2} + \frac{5788\lambda^2}{\lambda^2 - 2581^2} \tag{9}$$

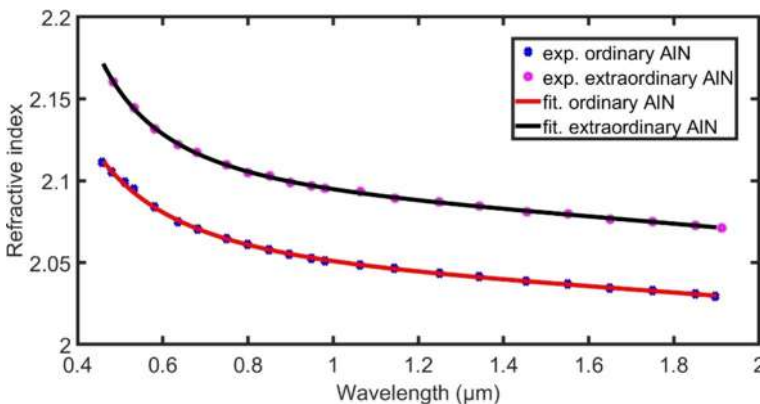
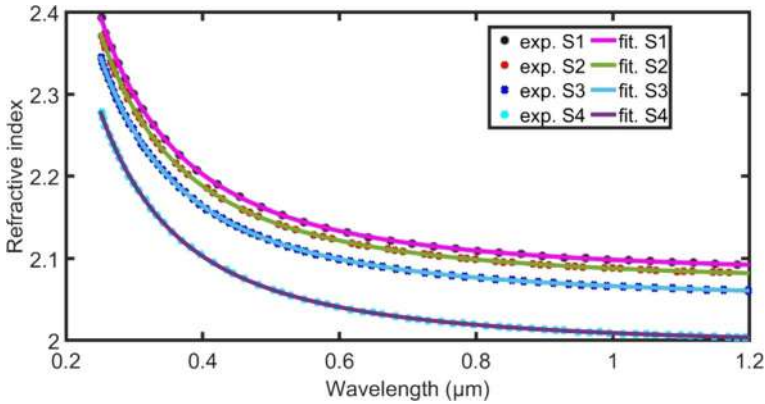


Fig. 4 Experimental (Bowman et al. 2018) and fitted ordinary and extraordinary RIs (using Eq. 6 and 7) of AIN versus the wavelengths from 0.46 to 1.90  $\mu\text{m}$



**Fig. 5** Experimental (Ababneh et al. 2020) and fitted RIs (using Eq. 8–11) of AlN versus the wavelengths from 0.25 to 1.20 μm at different sputtering setups

S3: At power of 1000 W, pressure of 0.4 Pa, 100%  $N_2$ , sputtering time of 1600 s, and thickness of 520 nm:

$$n^2 = -11.22294 + \frac{15.41658\lambda^2}{\lambda^2 - 0.07002^2} + \frac{-52860\lambda^2}{\lambda^2 - (-4868065)^2} \tag{10}$$

S4: At power of 1000 W, pressure of 0.6 Pa, 100%  $N_2$ , sputtering time of 1700s, and thickness of 470 nm:

$$n^2 = -9.47014 + \frac{13.43579\lambda^2}{\lambda^2 - 0.07242^2} + \frac{50671\lambda^2}{\lambda^2 - 13095^2} \tag{11}$$

Besides, Ababneh et al. (2020) studied the thickness effect on RI of AlN by sputtering samples at different sputtering times and fixed the other conditions (at the power of 1000 W, pressure of 0.4 Pa, and 100%  $N_2$ ). The coating chamber was filled with 100%  $N_2$  or a mixture of Ar and  $N_2$  (both of them with a purity of 99.999%). The mass flow controllers are used to adjust this process. Nominally, the substrates were not heated. They observed that the impact of the thickness change from 130 to 1060 nm can be neglected. The small change in RI is due to the change in the grain size and voids ratio (with the same density). We fitted the experimental results using the Sellmeier formula as follows (Fig. 6):

At a sputtering time of 400 s (thickness of 130 nm):

$$n^2 = -16.12276 + \frac{20.24648\lambda^2}{\lambda^2 - 0.06567^2} + \frac{1380899\lambda^2}{\lambda^2 - 38389222^2} \tag{12}$$

At a sputtering time of 1600 s (thickness of 520 nm):

$$n^2 = -15.63276 + \frac{19.82969\lambda^2}{\lambda^2 - 0.06176^2} + \frac{7888\lambda^2}{\lambda^2 - 1894^2} \tag{13}$$

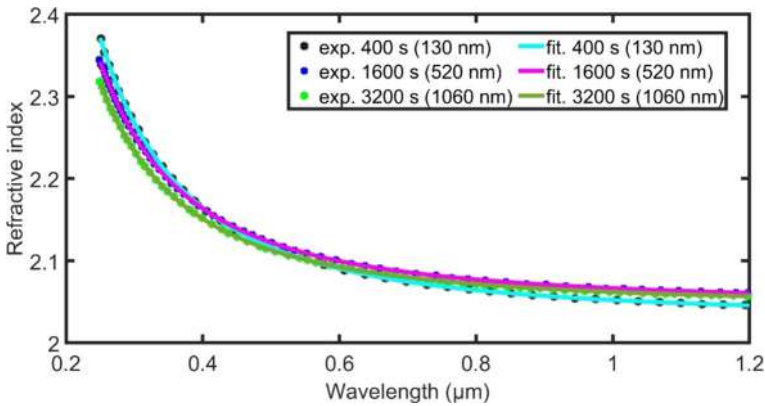


**Fig. 6** Experimental (Ababneh et al. 2020) and fitted RIs (using Eq. 12–14) of AlN versus the wavelengths from 0.25 to 1.20 μm at different sputtering times (different thicknesses)

At a sputtering time of 3200 s (thickness of 1060 nm):

$$n^2 = -13.88910 + \frac{18.07200\lambda^2}{\lambda^2 - 0.06199^2} + \frac{1373\lambda^2}{\lambda^2 - 1569^2} \tag{14}$$

Bui et al. (2015) deposited and analyzed wurtzite AlN films with different thicknesses. They measured the RI of wurtzite AlN films at different thicknesses during the growth process at 350 °C using ammonia (NH<sub>3</sub>) and trimethylaluminum (TMA) as precursors with pulse lengths of 4 s and 0.1 s, respectively, by thermal atomic layer deposition (ALD). The plasma power was 1.5 kW. AlN films were deposited on wafers of standard 4-in. Si(111) substrates. The pressure fluctuated from 0.9 to 1.2 mbar. It was observed that the RI strongly increased by increasing the thickness from 5 to 40 nm. For thicknesses from 40 to 70 nm, the RI slightly changes (seems constant or saturated). The film morphology, microstructure, and mass density may explain the strong dependence between thickness and RI. The RI of AlN drops with decreasing thickness, presumably due to decreasing density and a lack of homogeneity or continuity (Bosund et al. 2011). The slight increase in RI of films of AlN thicker than 30 nm is due to the higher carbon and lower oxygen concentrations in films (Alevli et al. 2012). We fitted the experimental results using the Sellmeir formula as follows (Fig. 7):

For 5 nm:

$$n^2 = 1.43999 + \frac{0.16225\lambda^2}{\lambda^2 - 0.25589^2} + \frac{-288\lambda^2}{\lambda^2 - 249^2} \tag{15}$$

For 10 nm:

$$n^2 = -31.52645 + \frac{33.71917\lambda^2}{\lambda^2 - 0.04188^2} + \frac{360913\lambda^2}{\lambda^2 - 15042^2} \tag{16}$$

For 20 nm:

$$n^2 = -55.12069 + \frac{58.12456\lambda^2}{\lambda^2 - 0.03528^2} + \frac{528594\lambda^2}{\lambda^2 - 8732^2} \tag{17}$$

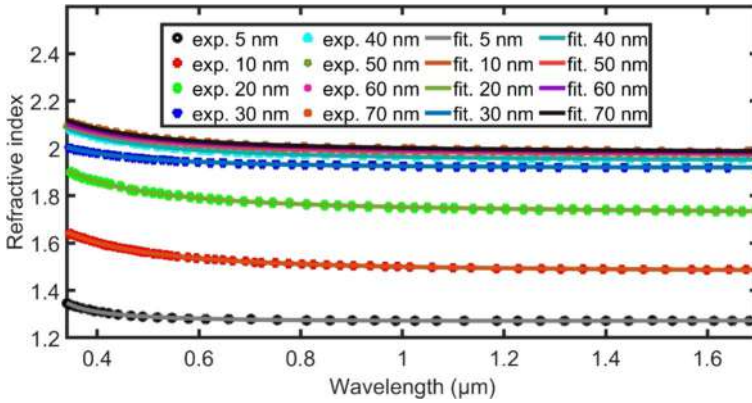


**Fig. 7** Experimental (Bui et al. 2015) and fitted RIs (using Eqs. 15–22) of AIN versus the wavelengths from 0.34 to 1.70 μm at different thicknesses growth by thermal mode at 350 °C

For 30 nm:

$$n^2 = -0.50046 + \frac{4.16746\lambda^2}{\lambda^2 - 0.09521^2} + \frac{-3514\lambda^2}{\lambda^2 - 1622^2} \tag{18}$$

For 40 nm:

$$n^2 = -24.11737 + \frac{27.91704\lambda^2}{\lambda^2 - 0.04699^2} + \frac{20033\lambda^2}{\lambda^2 - 2624^2} \tag{19}$$

For 50 nm:

$$n^2 = -56.62794 + \frac{60.51807\lambda^2}{\lambda^2 - 0.03114^2} + \frac{547946\lambda^2}{\lambda^2 - 11851^2} \tag{20}$$

For 60 nm:

$$n^2 = -59.58820 + \frac{63.52275\lambda^2}{\lambda^2 - 0.03008^2} + \frac{294633\lambda^2}{\lambda^2 - 5567^2} \tag{21}$$

For 70 nm:

$$n^2 = -60.14152 + \frac{64.09070\lambda^2}{\lambda^2 - 0.03112^2} + \frac{687411\lambda^2}{\lambda^2 - 10792^2} \tag{22}$$

Bui et al. (2014) deposited and characterized AIN films using thermal ALD from TMA and NH<sub>3</sub>. A completely covered substrate with AIN was obtained with sheets of around 2 nm thick. Standard substrates were 4-inch wafers of Si, covered with or without thermally grown SiO<sub>2</sub> film with a thickness of a 100-nm top layer. They noticed a strong dependence between growth temperature and thickness on the optical functions (n, k). They measured n(λ) and k(λ) during the growth process at 350 °C by thermal ALD using a Woollam M2000 spectroscopic ellipsometer. n(λ) increases significantly by increasing the thickness of AIN up to 40 nm. Then, n(λ) was saturated. They discussed that the RI of AIN decreases with the thickness decrease, which may be because of a lack of homogeneity or continuity

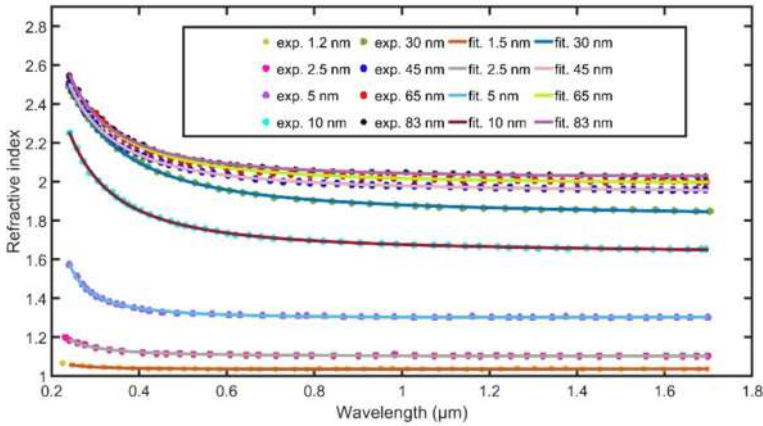


**Fig. 8** Experimental (Bui et al. 2014) and fitted RIs (using Eqs. 23–30) of AlN versus the wavelengths from 0.24 to 1.70 μm at different thicknesses

and the lower densities. We fitted the experimental results using the Sellmeier formula as follows (Fig. 8):

For 1.2 nm:

$$n^2 = 1.00924 + \frac{0.05932\lambda^2}{\lambda^2 - 0.16523^2} + \frac{-1262\lambda^2}{\lambda^2 - 755^2} \tag{23}$$

For 2.5 nm:

$$n^2 = 0.92932 + \frac{0.28281\lambda^2}{\lambda^2 - 0.15423^2} + \frac{-176\lambda^2}{\lambda^2 - (-373)^2} \tag{24}$$

For 5 nm:

$$n^2 = 1.16939 + \frac{0.50340\lambda^2}{\lambda^2 - 0.18919^2} + \frac{-854\lambda^2}{\lambda^2 - 345^2} \tag{25}$$

For 10 nm:

$$n^2 = -5.14923 + \frac{7.86467\lambda^2}{\lambda^2 - 0.11562^2} + \frac{10575\lambda^2}{\lambda^2 - 1005^2} \tag{26}$$

For 30 nm:

$$n^2 = -233.68663 + \frac{237.07654\lambda^2}{\lambda^2 - 0.02607^2} + \frac{902457\lambda^2}{\lambda^2 - (-8277)^2} \tag{27}$$

For 45 nm:

$$n^2 = -6.25002 + \frac{10.05581\lambda^2}{\lambda^2 - 0.10667^2} + \frac{0.02800\lambda^2}{\lambda^2 - 2.73670^2} \tag{28}$$

For 65 nm:

$$n^2 = -8.88337 + \frac{12.82962\lambda^2}{\lambda^2 - 0.09809^2} + \frac{-514713\lambda^2}{\lambda^2 - 29181704^2} \tag{29}$$

For 83 nm:

$$n^2 = -4.87036 + \frac{8.92497\lambda^2}{\lambda^2 - 0.11170^2} + \frac{-5390\lambda^2}{\lambda^2 - (-781)^2} \tag{30}$$

Besides, (Bui et al. 2014) studied the impact of growing temperatures. By increasing the growing temperatures from 330 to 350 °C and 370 °C,  $n(\lambda)$  increases remarkably, may due to the impurities of oxygen and/or carbon in the films, or due to density and the thermo-optic effect. We fitted the experimental results using the Sellmeir formula as follows (Fig. 9):

During growth at 330 °C:

$$n^2 = -2.40936 + \frac{6.17751\lambda^2}{\lambda^2 - 0.12510^2} + \frac{10877\lambda^2}{\lambda^2 - 1027^2} \tag{31}$$

During growth at 350 °C:

$$n^2 = -4.12184 + \frac{8.07380\lambda^2}{\lambda^2 - 0.11660^2} + \frac{31114\lambda^2}{\lambda^2 - 2114^2} \tag{32}$$

During growth at 370 °C:

$$n^2 = -50.23771 + \frac{54.30590\lambda^2}{\lambda^2 - 0.05298^2} + \frac{42082\lambda^2}{\lambda^2 - 3911^2} \tag{33}$$

In addition, Bui et al. (2014) grew an AlN film with a thickness of 100 nm at 350 °C. They measured the RI of this film at different temperatures (150 °C, 250 °C, 350 °C, and 450 °C). The density of AlN films increases when they grow at high temperatures. This increase in the density causes a slight increase in RI (Watanabe et al. 2008), as clear in Fig. 10. We fitted the experimental results using the Sellmeir formula as follows:

Measured at 150 °C:

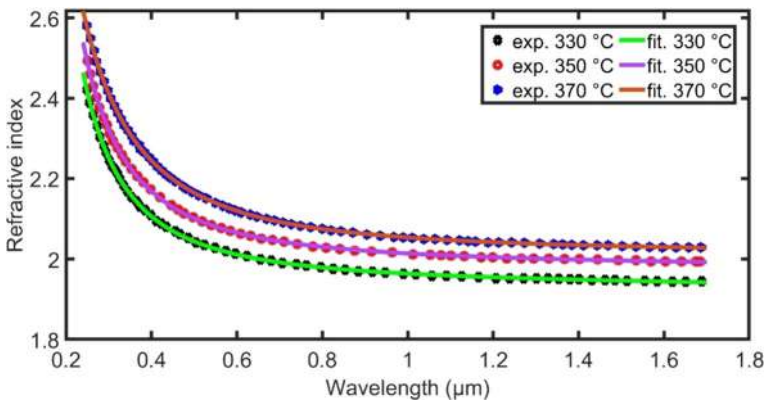


**Fig. 9** Experimental (Bui et al. 2014) and fitted RIs (using Eqs. 31–33) of 60 nm thick of AlN versus the wavelengths from 0.24 to 1.70 μm grown at 330 °C, 350 °C and 370 °C

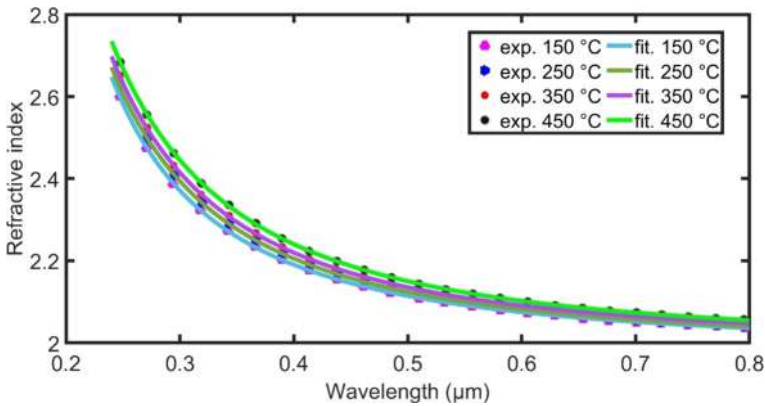


**Fig. 10** Experimental (Bui et al. 2014) and fitted RIs (using Eqs. 34–37) of 100 nm thick of AlN versus the wavelengths from 0.24 μm to 0.80 μm grown at 350 °C, and measured at 150 °C, 250 °C, 350 °C, and 450 °C

$$n^2 = -2.26978 + \frac{6.23442\lambda^2}{\lambda^2 - 0.13751^2} + \frac{3434\lambda^2}{\lambda^2 - (-465)^2} \tag{34}$$

Measured at 250 °C:

$$n^2 = -3.83652 + \frac{7.79133\lambda^2}{\lambda^2 - 0.12925^2} + \frac{301144\lambda^2}{\lambda^2 - (-19315621)^2} \tag{35}$$

Measured at 350 °C:

$$n^2 = -4.58497 + \frac{8.55798\lambda^2}{\lambda^2 - 0.12667^2} + \frac{2414516\lambda^2}{\lambda^2 - (-1683917190)^2} \tag{36}$$

Measured at 450 °C:

$$n^2 = -6.46131 + \frac{10.44380\lambda^2}{\lambda^2 - 0.12017^2} + \frac{75871202\lambda^2}{\lambda^2 - 23461306^2} \tag{37}$$

Bosund et al. (2011) examined the effect of growth temperature on the RI of AlN film 100 nm thick from 100 to 300 °C. They observed that a crystalline AlN film was grown at 300 °C, whereas amorphous films were grown at lower growth temperatures. As clear in Fig. 11, decreasing growth temperature (increasing hydrogen concentration) decreases mass density and RI. We fitted the experimental results using the Sellmeir formula as follows (Fig. 11):

For growth temperature of 100 °C:

$$n^2 = -44.57570 + \frac{47.37304\lambda^2}{\lambda^2 - 0.04056^2} + \frac{-0.00306\lambda^2}{\lambda^2 - (-1.92144)^2} \tag{38}$$

For growth temperature of 150 °C:

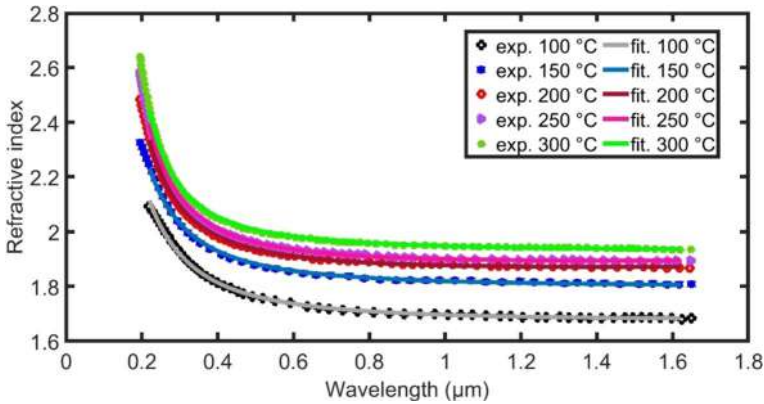


**Fig. 11** Experimental (Bosund et al. 2011) and fitted RIs (using Eqs. 38–42) of 100 nm thick AlN versus the wavelengths from 0.22 μm to 1.62 μm grown at 100 °C, 150 °C, 200 °C, 250 °C, and 300 °C

$$n^2 = -12.82506 + \frac{16.05909\lambda^2}{\lambda^2 - 0.06880^2} + \frac{-405660\lambda^2}{\lambda^2 - (-14000328)^2} \tag{39}$$

For growth temperature of 200 °C:

$$n^2 = -3.37474 + \frac{6.80123\lambda^2}{\lambda^2 - 0.10548^2} + \frac{-2591\lambda^2}{\lambda^2 - 370^2} \tag{40}$$

For growth temperature of 250 °C:

$$n^2 = -2.01382 + \frac{5.53193\lambda^2}{\lambda^2 - 0.11757^2} + \frac{-38235\lambda^2}{\lambda^2 - (-1547)^2} \tag{41}$$

For growth temperature of 300 °C:

$$n^2 = -0.56682 + \frac{4.28935\lambda^2}{\lambda^2 - 0.12893^2} + \frac{-69934109\lambda^2}{\lambda^2 - 139724270^2} \tag{42}$$

Shi et al. (2021) deposited films of polycrystalline AlN on Si wafers (111) at 25 °C with thicknesses of 106 nm, 222 nm, and 520 nm, using reactive magnetron sputtering in Ar/N<sub>2</sub> atmosphere from an Al target (~99.99% purity). The base pressure of sputtering chamber was 1 × 10<sup>-6</sup> Torr. The deposition process occurred at 3.7 × 10<sup>-3</sup> Torr and 25 °C, 40/5 (sccm) in Ar/N<sub>2</sub> flow, 300 W in RF power or 3.75 W/cm<sup>2</sup> in power density. The discharge was driven at 13.56 MHz. The rate of deposition was 2.3 nm/min. As the thickness of AlN films increased from 106 nm, 222 nm, and 520 nm, the roughness of the surface increased. The extinction coefficients of prepared samples are zero at wavelengths from 0.38 to 0.78 μm. They also studied the RIs of these films at this wavelength range. The RI fluctuation was due to the growth process stability (Ababneh et al. 2020; Shi et al. 2021). The unstable growth process affected the film crystallinity, which led to significant scattering of visible light and RI fluctuations. The RIs of 520 nm and 222 nm films were extremely close to one another, suggesting that the growth of 520 nm and 200 nm was relatively stable. The different behavior of 222 nm film is due to the small amount of oxygen expressed as AlN<sub>0.82</sub>O<sub>0.19</sub> (Shi et al. 2021; Kuang et al. 2012).

We fitted the experimental results using the Sellmeir formula as follows (Fig. 12):

For a thickness of 106 nm:

$$n^2 = 3.02826 + \frac{0.48419\lambda^2}{\lambda^2 - 0.31537^2} + \frac{-5844137\lambda^2}{\lambda^2 - 6517910^2} \tag{43}$$

For a thickness of 106 nm:

$$n^2 = 3.12469 + \frac{0.75103\lambda^2}{\lambda^2 - 0.24708^2} + \frac{1120\lambda^2}{\lambda^2 - 175^2} \tag{44}$$

For a thickness of 106 nm:

$$n^2 = 1.50305 + \frac{2.27032\lambda^2}{\lambda^2 - 0.16427^2} + \frac{-106\lambda^2}{\lambda^2 - (-89)^2} \tag{45}$$

Choudhary et al. (2013) studied the RIs of wurtzite AlN by depositing different thicknesses on a Si (100) substrate using a system of reactive pulsed DC balanced magnetron sputtering coupled with asymmetric bipolar DC generator. The target material was aluminum, with a purity of 99.99%. The substrate temperature was about 100 °C. The working pressure of the deposition process was  $1.5 \times 10^{-3}$  mbar in nitrogen and argon atmosphere. Deposition base pressure, cathode power density, Pulse frequency, duty cycle, target-to-substrate distance, and total gas (Ar + N<sub>2</sub>) flow rate were  $1.1 \times 10^{-5}$  mbar, 3.3 W/cm<sup>2</sup>, 125 kHz, 75%, 7.5 cm, and 10 sccm, respectively. They controlled the thickness by changing the deposition conditions, such as the nitrogen/argon flow ratio. The irregular change in RI with the thickness of films was due to the presence of oxygen in the samples (Choudhary et al. 2013). For a nitrogen/argon flow ratios higher than 50%, AlN RI was changed from 1.67 to 1.84 due to the porous nature of films. For nitrogen/argon flow ratios lower than 50%, AlN RI decreased due to the growth of non-stoichiometric layers (Borges et al. 2013)

We fitted the experimental results as follows (Fig. 13):

For 196 nm (40% N<sub>2</sub>):

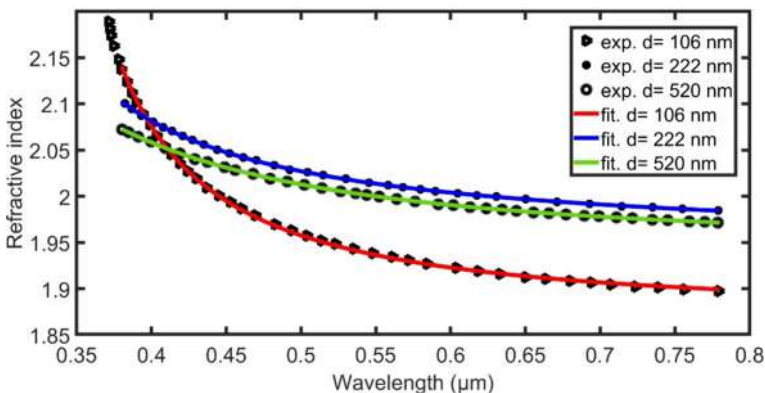
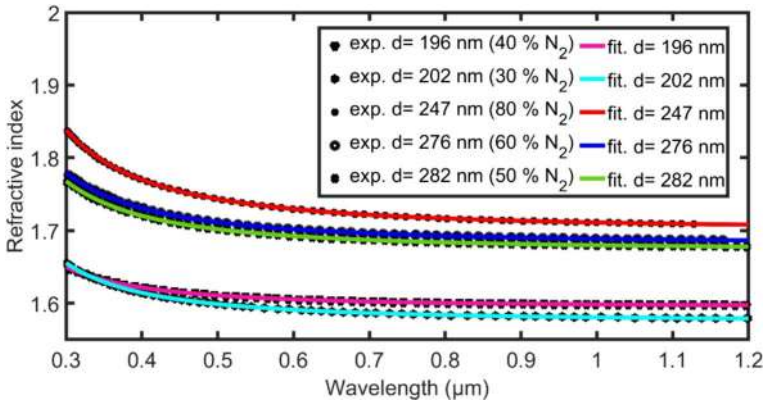


Fig. 12 Experimental (Shi et al. 2021) and fitted RIs (using Eqs. 43–45) for different thick AlN films versus the wavelengths from 0.38 μm to 0.78 at 25 °C



**Fig. 13** Experimental (Choudhary et al. 2013) and fitted RIs (using Eqs. 46–50) for different thick AlN films versus the wavelengths from 0.30 to 1.20 μm

$$n^2 = 1.99924 + \frac{0.54139\lambda^2}{\lambda^2 - 0.15027^2} + \frac{-96\lambda^2}{\lambda^2 - 238^2} \tag{46}$$

For 202 nm (30% N<sub>2</sub>):

$$n^2 = 1.78374 + \frac{0.69693\lambda^2}{\lambda^2 - 0.15639^2} + \frac{-23\lambda^2}{\lambda^2 - 288^2} \tag{47}$$

For 247 nm (80% N<sub>2</sub>):

$$n^2 = 1.47698 + \frac{1.41807\lambda^2}{\lambda^2 - 0.15133^2} + \frac{196676\lambda^2}{\lambda^2 - (-5445826)^2} \tag{48}$$

For a thickness of 276 nm (60% N<sub>2</sub>):

$$n^2 = 1.65134 + \frac{1.17522\lambda^2}{\lambda^2 - 0.14190^2} + \frac{-599\lambda^2}{\lambda^2 - 748^2} \tag{49}$$

For a thickness of 282 nm (50% N<sub>2</sub>):

$$n^2 = 1.75455 + \frac{1.04370\lambda^2}{\lambda^2 - 0.14649^2} + \frac{-24\lambda^2}{\lambda^2 - 156^2} \tag{50}$$

Khoshman and Kordesch (2005) analyzed and measured the RIs of amorphous AlN with a thickness of 120 nm sputtered on Si (111) at T < 325 K at a wavelength from 0.3 to 1.4 μm. An Al target with purity of 99.999% in a pure nitrogen atmosphere was used. The base pressure of the deposition system was in the range from 4 × 10<sup>-7</sup> to 6 × 10<sup>-7</sup> Torr while the sputtering pressure was fixed at 5 × 10<sup>-3</sup> Torr. The RF sputtering power was 139 W.

We fitted the experimental results as follows (Fig. 14):

$$n^2 = -0.74895 + \frac{4.17165\lambda^2}{\lambda^2 - 0.13651^2} + \frac{2451070\lambda^2}{\lambda^2 - 32889369^2} \tag{51}$$

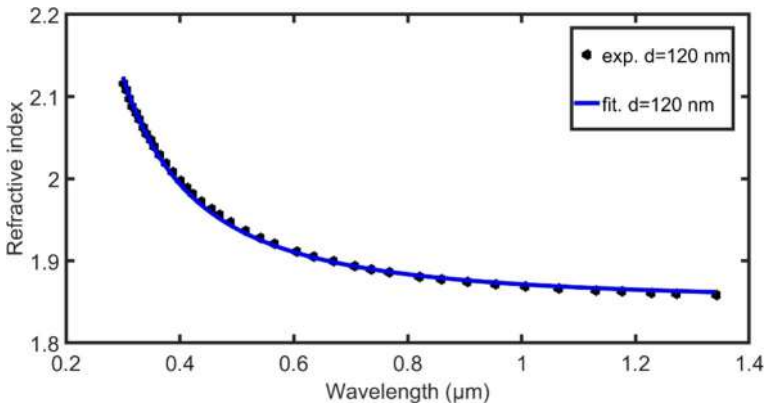


**Fig. 14** Experimental (Khoshman and Kordesch 2005) and fitted RI (using Eq. 51) for AlN film versus the wavelength

Alsaad et al. (2020) deposited textured-wurtzite AlN films on glass substrates of thickness 550 nm by changing the back pressure during the DC-magnetron sputtering process. Deposition chamber was evacuated in an ultra-clean medium at  $1 \times 10^{-5}$  Pa, and contained a 100%  $N_2$  gas. The plasma power was set to 300 W. The RI significantly decreases with increasing the back pressure due to decreasing the charge carrier density (Fasasi et al. 2018), as clear in Fig. 15.

We fitted the experimental results as follows:

With back pressure 0.2 Pa:

$$n^2 = -16.42134 + \frac{20.93417\lambda^2}{\lambda^2 - 0.06010^2} + \frac{201999\lambda^2}{\lambda^2 - 8952850^2} \tag{52}$$

With back pressure 0.4 Pa:

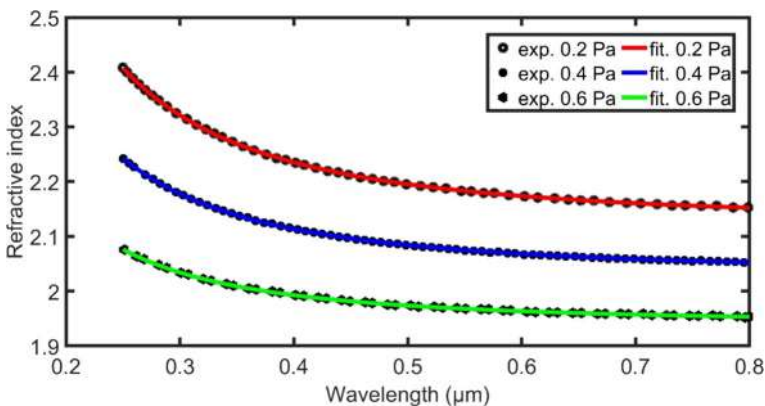


**Fig. 15** Experimental (Alsaad et al. 2020) and fitted RIs (using Eqs. 52–54) for 550 nm thick AlN films at different back pressures versus the wavelength from 0.25 to 0.80  $\mu\text{m}$

$$n^2 = -8.04519 + \frac{12.174829\lambda^2}{\lambda^2 - 0.06567^2} + \frac{17824327\lambda^2}{\lambda^2 - (-15943663)^2} \tag{53}$$

With back pressure 0.6 Pa:

$$n^2 = -5.73259 + \frac{9.49672\lambda^2}{\lambda^2 - 0.05834^2} + \frac{6904728\lambda^2}{\lambda^2 - (-2789981)^2} \tag{54}$$

In 2007, Baek et al. (2007) deposited and optically characterized polycrystalline AlN thin films onto sapphire (0001) at different substrate temperatures using pulsed laser deposition (PLD). A turbo-molecular pump was used to evacuate the system to a base pressure of  $1.3 \times 10^{-6}$  Pa. The distance between the target and temperature-controlled substrate was 5.1 cm for most samples. The thickness of the samples was non-uniform. Baek et al. (2007) confirmed that the RI of AlN films depends on laser fluence rather than simply on substrate temperature and deposition rate. By fitting the experimental results, we get matched equations as follows (Fig. 16):

For low laser fluence, deposition rate of 20 nm/min, maximum laser fluence of 2 J/cm<sup>2</sup>, substrate temperature of 300 °C, thickness of 492 nm:

$$n^2 = 2.08415 + \frac{2.70697\lambda^2}{\lambda^2 - 0.14339^2} + \frac{0.01637\lambda^2}{\lambda^2 - 1.14474^2} \tag{55}$$

For high laser fluence, deposition rate of 30 nm/min, maximum laser fluence of 7.8 J/cm<sup>2</sup>, substrate temperature of 500 °C, thickness of 1499 nm:

$$n^2 = 1.98043 + \frac{2.25779\lambda^2}{\lambda^2 - 0.14348^2} + \frac{0.00871\lambda^2}{\lambda^2 - (-1.09832)^2} \tag{56}$$

Venkataraj et al. (2006) sputtered AlN films on Si (100) and glass using reactive DC magnetron sputtering at different N<sub>2</sub> flow (0–8 sccm) at room temperature. Target substrate distance, cathode current, and pressure were 55 mm, 500 mA and 0.8 Pa, respectively. They have established that crystalline AlN can be manufactured for N<sub>2</sub> flows higher than 4.75 sccm. They analyzed the RIs of AlN films at 4.75 sccm and 5 sccm over photon

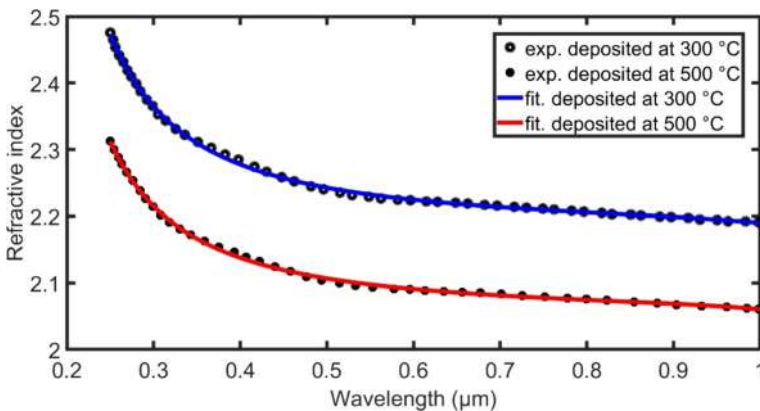


**Fig. 16** Experimental (Baek et al. 2007) and fitted RIs (using Eqs. 55 and 56) at different substrate temperatures versus wavelengths from 0.25 to 1.00 μm

energy from 0 to 6 eV. As clear in Fig. 17, there was a small change in RI upon increasing  $N_2$  flow due to the change in the density of the films. By fitting the experimental results, we get matched equations at a wavelength from 0.2 to 42,000  $\mu\text{m}$  (above this wavelength,  $n$  is constant; 1.94 for 4.75 sccm and 1.85 for 5.0 sccm) as follows (Fig. 17):

For 4.75 sccm (Real part):

$$n^2 = (3.35121 - 1.50233 \times 10^{-5}i) + \frac{(0.21182 + 0.72551i)\lambda^2}{\lambda^2 - (0.18102 - 0.06627i)^2} + \frac{(0.21182 - 0.72549i)\lambda^2}{\lambda^2 - (0.18102 + 0.06627i)^2} \tag{57}$$

For 5.0 sccm (Real part):

$$n^2 = (-9.69421 + 0.00125i) + \frac{(12.90912 - 0.00121i)\lambda^2}{\lambda^2 - (0.07780 + 2.73756 \times 10^{-6}i)^2} + \frac{(0.20378 - 4.03710e - 05i)\lambda^2}{\lambda^2 - (3.40653 \times 10^{-5} - 0.38698i)^2} \tag{58}$$

Larciprete et al. (2006) studied the ordinary and extraordinary RIs ( $n_o$  and  $n_e$ ) of wurtzite AlN films sputtered onto silicon substrate at ambient temperature. There is a discrepancy between the experimental and calculated data for ne because the experimental data were a mix for two thicknesses of 1496 nm or 1940 nm. By fitting the measured results, we get matched equations at a wavelength from 0.4 to 0.8  $\mu\text{m}$  as follows (Fig. 18):

For ordinary RI with a thickness of 1496 nm:

$$n^2 = -1.86315 + \frac{3.02032\lambda^2}{\lambda^2 - 0.23431^2} + \frac{19253642\lambda^2}{\lambda^2 - (-16913613)^2} \tag{59}$$

For ordinary RI with a thickness of 1940 nm:

$$n^2 = -2.04579 + \frac{3.23143\lambda^2}{\lambda^2 - 0.22941^2} + \frac{9344413\lambda^2}{\lambda^2 - (-8119614)^2} \tag{60}$$

For extraordinary RI with a thickness of 1496 or 1940 nm:

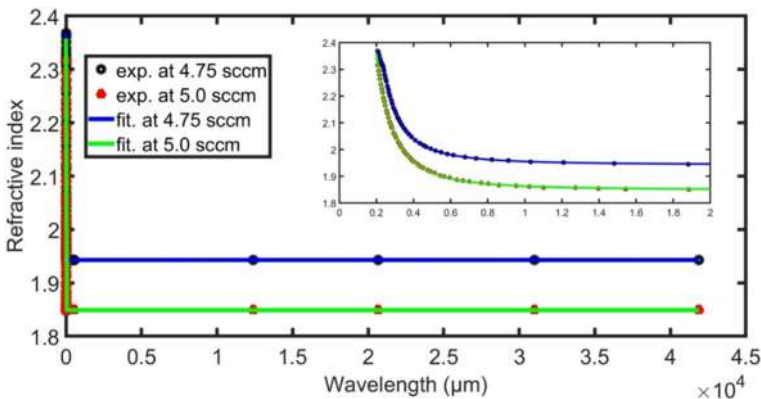
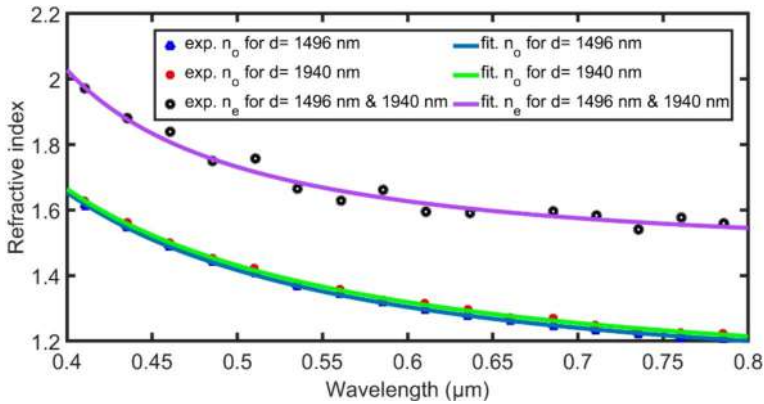


Fig. 17 Experimental (Venkataraj et al. 2006) and fitted RIs (using Eqs. 57 and 58) at different  $N_2$  flow (0 sccm–8 sccm) versus the wavelength



**Fig. 18** Measured (Larciprete et al. 2006) and fitted RIs (using Eqs. 59–61) at different thicknesses for different polarization states versus wavelengths from 0.40 to 0.80 μm

$$n^2 = 0.61642 + \frac{1.52135\lambda^2}{\lambda^2 - 0.30061^2} + \frac{192957019\lambda^2}{\lambda^2 - (-125280841)^2} \tag{61}$$

In 2021, Ababneh et al. (2021) calculated the RIs of wurtzite AlN films (thickness of 500 nm) by depositing films on substrates of glass at different sputtering pressures and at or near room temperature. The target was Al, with a diameter of 200 mm and purity of 99.999%, at a distance of 65 mm from the unheated substrate. During the process of sputtering, the plasma power was 1000 W, and 100% of N<sub>2</sub> atmosphere was pumped into the deposition chamber. The pressure of sputtering process was changed between 2 × 10<sup>-3</sup> mbar and 6 × 10<sup>-3</sup> mbar. By fitting the measured results, we get matched equations at a wavelength from 0.25 to 0.8 μm as follows (Fig. 19):

At 2 × 10<sup>-3</sup> mbar:

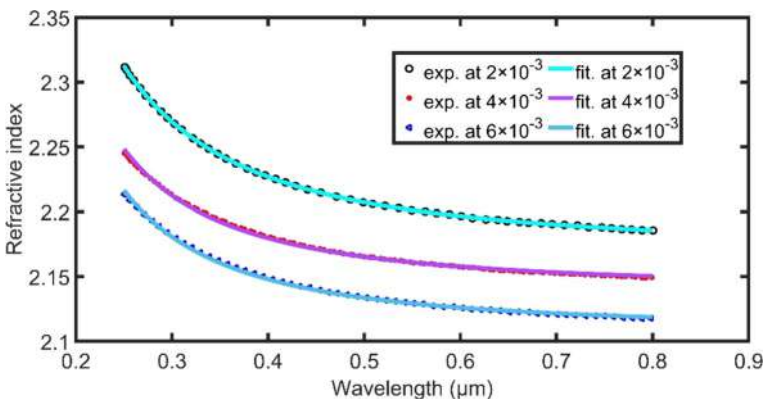


**Fig. 19** Measured (Ababneh et al. 2021) and fitted RIs (using Eqs. 62–64) at different sputtering pressures versus the wavelength

$$n^2 = -8.85361 + \frac{13.57625\lambda^2}{\lambda^2 - 0.05245^2} + \frac{4740\lambda^2}{\lambda^2 - 864^2} \tag{62}$$

At  $4 \times 10^{-3}$  mbar:

$$n^2 = 1.86943 + \frac{2.71491\lambda^2}{\lambda^2 - 0.09616^2} + \frac{3670922\lambda^2}{\lambda^2 - (-3903717903)^2} \tag{63}$$

At  $6 \times 10^{-3}$  mbar:

$$n^2 = 1.79718 + \frac{2.65265\lambda^2}{\lambda^2 - 0.09643^2} + \frac{187675396\lambda^2}{\lambda^2 - (-24257341)^2} \tag{64}$$

Shin et al. (2021) designed AlN with a thickness of 550 nm on sapphire as a microring resonator using  $Cl_2/Ar$  based inductive coupled plasma reactive ion etching. E-beam lithography was used to define microring resonator patterns using two layers of hard mask. More experimental details are listed in Ref. (Shin et al. 2021). By fitting the measured RIs, we get matched equations at a wavelength from 0.25 to 1.6  $\mu\text{m}$  as follows (Fig. 20):

For  $n_o$ :

$$n^2 = 1.18842 + \frac{2.98798\lambda^2}{\lambda^2 - 0.14114^2} + \frac{-155\lambda^2}{\lambda^2 - 230^2} \tag{65}$$

For  $n_e$ :

$$n^2 = 2.18784 + \frac{2.28349\lambda^2}{\lambda^2 - 0.15758^2} + \frac{-2654\lambda^2}{\lambda^2 - 598^2} \tag{66}$$

Atluri (2020) deposited crystalline AlN on a silicon wafer with thermal oxide using reactively sputtering Al at a substrate temperature of 200 °C, gas flow of 20 sccm, and base pressure of  $10^{-6}$  Torr. Using Spectroscopic ellipsometry, Atluri measured the RIs of AlN at different gas flow ratios (Argon/Nitrogen). By changing the gas flow ratio, there is a slight shift in the RI of AlN, as clear in Fig. 21. By fitting the measured RIs, we get matched equations at a wavelength from 0.3  $\mu\text{m}$  to 1.7  $\mu\text{m}$  as follows:

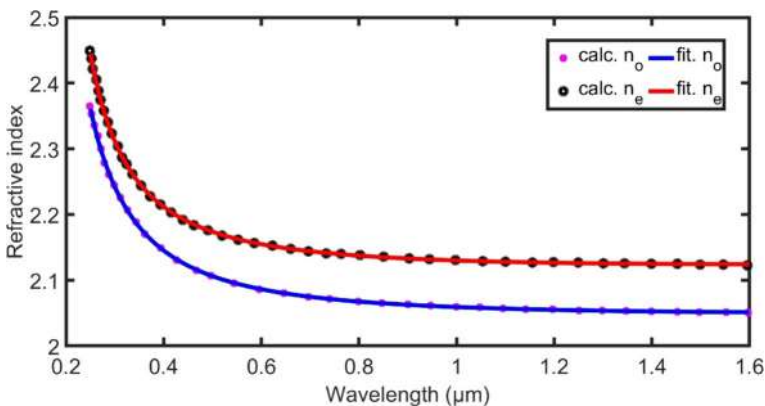


Fig. 20 Measured (Shin et al. 2021) and fitted RIs (using Eqs. 65 and 66) at different sputtering pressures versus wavelengths

At Argon/Nitrogen ratio of 70:30, film thickness of 67.99 nm, and roughness of 4.88 nm:

$$n^2 = 1.73222 + \frac{1.95565\lambda^2}{\lambda^2 - 0.16450^2} + \frac{100\lambda^2}{\lambda^2 - 63^2} \tag{67}$$

At Argon/Nitrogen ratio of 60:40, film thickness of 64.57 nm, and roughness of 4.35 nm:

$$n^2 = 2.05898 + \frac{1.55965\lambda^2}{\lambda^2 - 0.17719^2} + \frac{266\lambda^2}{\lambda^2 - 102^2} \tag{68}$$

At Argon/Nitrogen ratio of 50:50, film thickness of 60.47, and roughness of 1.84 nm:

$$n^2 = 2.02395 + \frac{1.59214\lambda^2}{\lambda^2 - 0.17321^2} + \frac{0.23541\lambda^2}{\lambda^2 - 4.02555^2} \tag{69}$$

Besides, Atluri (2020) studied the impact of radio frequency (RF) sputtering power from 150 to 200 W on RI of AlN deposited on silicon wafers with thermal oxide at a constant nitrogen/argon ratio (70:30). Atluri noticed that the deposition rate and crystallinity increases with increasing the RF sputtering power. The RI of AlN slightly changes with increasing the RF sputtering power, as clear in Fig. 22. By fitting the measured RIs, we get matched equations at a wavelength from 0.3 to 1.7 μm as follows:

At 150 W, the thickness of 67.99 nm and roughness of 4.88 nm:

$$n^2 = 1.89229 + \frac{1.81875\lambda^2}{\lambda^2 - 0.17572^2} + \frac{21\lambda^2}{\lambda^2 - 27^2} \tag{70}$$

At 175 W, a thickness of 73.70 nm and roughness of 3.48 nm:

$$n^2 = 1.65550 + \frac{1.99500\lambda^2}{\lambda^2 - 0.16974^2} + \frac{21\lambda^2}{\lambda^2 - 26^2} \tag{71}$$

At 200 W, a thickness of 88.85 nm and roughness of 4.96 nm:

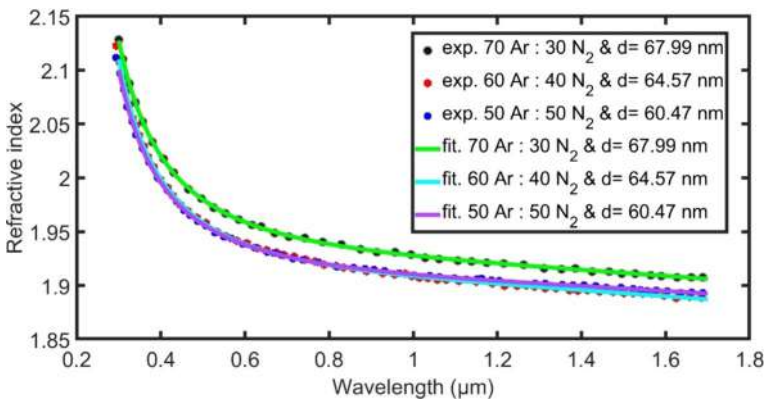


**Fig. 21** Measured (Atluri, 2020) and fitted RIs (using Eqs. 67–69) at different gas flow ratios (Argon/Nitrogen) versus the wavelength

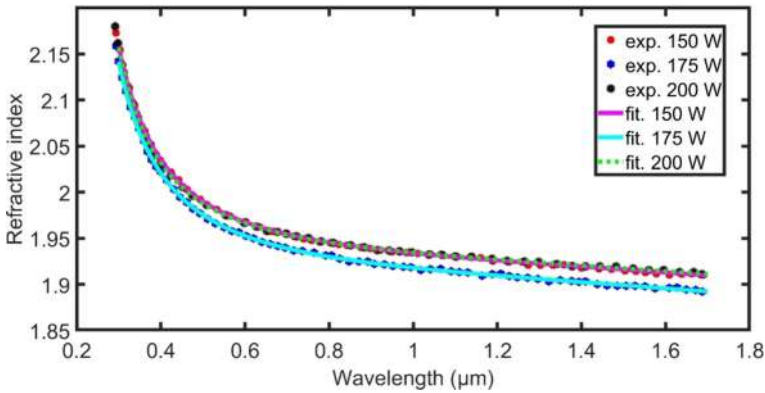


**Fig. 22** Measured (Atluri, 2020) and fitted RIs (using Eqs. 70–72) at different RF sputtering power versus the wavelength

$$n^2 = 2.18199 + \frac{1.53477\lambda^2}{\lambda^2 - 0.18473^2} + \frac{39\lambda^2}{\lambda^2 - 37^2} \tag{72}$$

In addition, Atluri (2020) investigated the effect of changing the sputtering pressure from 1 mTorr (mT) to 5 mT on the deposited AlN. He fixed the ratio of nitrogen/argon at 70:30 and the sputtering power at 200W. The RI of AlN decreases with an increase in the sputtering pressure, as clear in Fig. 23. By fitting the measured RIs, we get matched equations at a wavelength from 0.3 to 1.7  $\mu\text{m}$  as follows:

At 1 mT, the thickness of 140.09 nm and roughness of 3.30 nm:

$$n^2 = 1.72162 + \frac{2.35480\lambda^2}{\lambda^2 - 0.16287^2} + \frac{312\lambda^2}{\lambda^2 - 102^2} \tag{73}$$

At 3 mT, a thickness of 88.85 nm, and roughness of 4.96 nm:

$$n^2 = 1.73195 + \frac{1.96824\lambda^2}{\lambda^2 - 0.17091^2} + \frac{0.15949\lambda^2}{\lambda^2 - 3.36816^2} \tag{74}$$

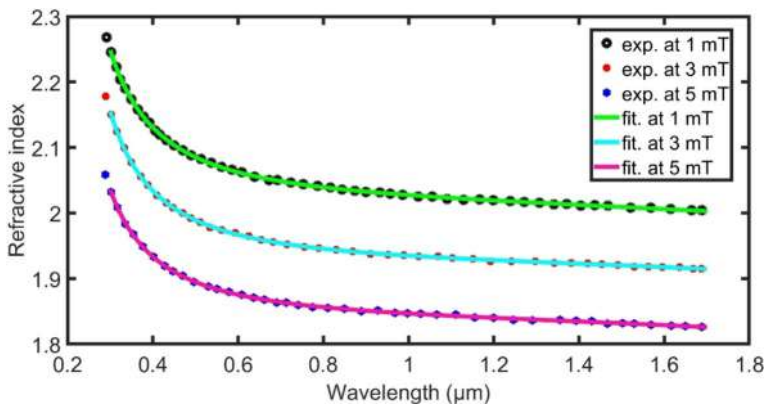


**Fig. 23** Measured (Atluri, 2020) and fitted RIs (using Eqs. 73–75) at different sputtering pressure versus wavelengths

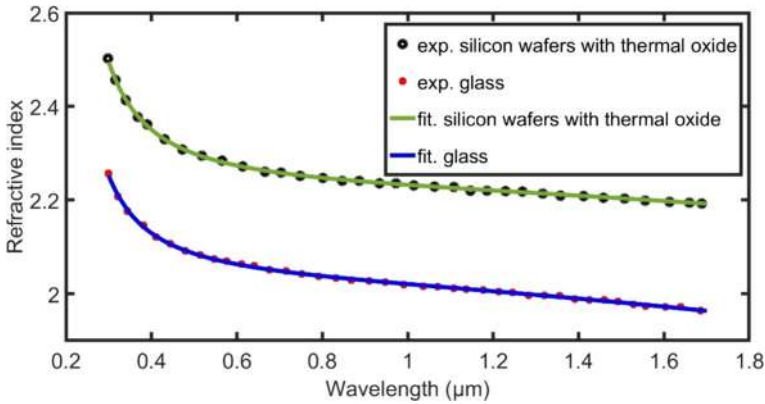


**Fig. 24** Measured (Atluri, 2020) and fitted RIs (using Eqs. 73–75) at different substrates versus the wavelength

At 5 mT, a thickness of 71.31 nm, and roughness of 3.33 nm:

$$n^2 = 1.624200 + \frac{1.75421\lambda^2}{\lambda^2 - 0.16548^2} + \frac{0.18512\lambda^2}{\lambda^2 - 3.39830^2} \tag{75}$$

Then, Atluri (Takikawa et al. 2001) studied the RIs of AlN deposited on different substrates (soda-lime glass and silicon wafers with thermal oxide). By changing the substrate, the phase of the film changed. The nanocrystalline film was created on a silicon wafer with thermal oxide, but an amorphous one was created on a glass substrate. By fitting the measured RIs, we get matched equations at a wavelength from 0.3 to 1.7 μm as follows (Fig. 24):

For silicon wafers with thermal oxide substrate:

$$n^2 = 2.94076 + \frac{2.03902\lambda^2}{\lambda^2 - 0.18501^2} + \frac{153\lambda^2}{\lambda^2 - 47^2} \tag{76}$$

For soda-lime glass substrate:

$$n^2 = 2.57490 + \frac{1.55553\lambda^2}{\lambda^2 - 0.18466^2} + \frac{33022\lambda^2}{\lambda^2 - (-569)^2} \tag{77}$$

### 3 Conclusion

The paper introduced new equations for calculating the RI of AlN, which makes it a significant contribution to modeling materials' optical properties. The RIs of AlN films with different geometries, phases, and different preparing and measuring conditions are widely discussed. The RI of AlN films over wavelength range from 0.2 to 42,000 μm are fitted, coded, and plotted. For wavelengths above 42,000 μm, the RI can be considered constant. Besides, the effect of thickness, measuring temperature, growth temperature, N<sub>2</sub> flow ratio, sputtering power, sputtering back pressure, and substrate on the RI of AlN are discussed and fitted. The impact of the thickness change from 130 to 1060 nm on the RI may be neglected. The RI strongly increased by increasing the thickness up to ~ 40 nm. The density of AlN films increases when they grow at high temperatures, and the RI slightly increases. Finally, the fitted RI equations are very useful for optical simulations. In future research, we will continue with other materials.

**Funding** The current work was assisted financially to the Dean of Science and Research at King Khalid University via the Large Group Project under grant number RGP. 2/46/45.

**Data availability** Requests for materials or code should be addressed to Zaky A. Zaky.

## Declarations

**Conflict of interest** The authors declare that they have no known competing financial interests or personal relationships that could have appeared to influence the work reported in this paper.

**Animals or human participants** This article does not contain any studies involving animals or human participants performed by any authors.

## References

- Ababneh, A., Albataineh, Z., Dagamseh, A., Al-Kofahi, I., Schäfer, B., Zengerle, T., et al.: Optical characterization of sputtered aluminum nitride thin films—correlating refractive index with degree of c-axis orientation. *Thin Solid Films* **693**, 137701 (2020). <https://doi.org/10.1016/j.tsf.2019.137701>
- Ababneh, A., Dagamseh, A., Albataineh, Z., Tantawi, M., Al-Bataineh, Q., Telfah, M., et al.: Optical and structural properties of aluminium nitride thin-films synthesized by DC-magnetron sputtering technique at different sputtering pressures. *Microsyst. Technol.* **27**, 3149–3159 (2021). <https://doi.org/10.1007/s00542-020-05081-4>
- Alevli, M., Ozgit, C., Donmez, I., Biyikli, N.: Structural properties of AlN films deposited by plasma-enhanced atomic layer deposition at different growth temperatures. *Physica Status Solidi (a)* **209**, 266–271 (2012). <https://doi.org/10.1002/pssa.201127430>
- Alsaad, A., Al-Bataineh, Q.M., Qattan, I., Ahmad, A.A., Ababneh, A., Albataineh, Z., et al.: Measurement and ab initio investigation of structural, electronic, optical, and mechanical properties of sputtered aluminum nitride thin films. *Front. Phys.* **8**, 115 (2020). <https://doi.org/10.3389/fphy.2020.00115>
- Ashrafi, T.M., Mohanty, G.: High-performance SPR sensor using wurtzite nitride semiconductors and TMDC: a comparative study. *Plasmonics* **19**, 817–823 (2024). <https://doi.org/10.1007/s11468-023-02038-x>
- Atluri, S.S.: Deposition and characterization of indium nitride and aluminum nitride thin films by reactive sputtering. Old Dominion University, Norfolk (2020)
- Baek, J., Ma, J., Becker, M.F., Keto, J.W., Kovar, D.: Correlations between optical properties, microstructure, and processing conditions of Aluminum nitride thin films fabricated by pulsed laser deposition. *Thin Solid Films* **515**, 7096–7104 (2007). <https://doi.org/10.1016/j.tsf.2007.03.003>
- Boey, F., Tok, A.: Porous AlN ceramic substrates by reaction sintering. *J. Mater. Process. Technol.* **140**, 413–419 (2003). [https://doi.org/10.1016/S0924-0136\(03\)00829-X](https://doi.org/10.1016/S0924-0136(03)00829-X)
- Borges, J., Barradas, N. P., Alves, E.: Influence of stoichiometry and structure on the optical properties of AlN<sub>x</sub>O<sub>y</sub> films. *J. Phys.* **46**, 1–11 (2013)
- Bosund, M., Sajavaara, T., Laitinen, M., Huhtio, T., Putkonen, M., Airaksinen, V.-M., et al.: Properties of AlN grown by plasma enhanced atomic layer deposition. *Appl. Surf. Sci.* **257**, 7827–7830 (2011). <https://doi.org/10.1016/j.apsusc.2011.04.037>
- Bowman, S.R., Brown, C.G., Taczak, B.: Optical dispersion and phase matching in gallium nitride and aluminum nitride. *Opt. Mater. Express* **8**, 1091–1099 (2018). <https://doi.org/10.1364/OME.8.001091>
- Carlone, C., Lakin, K., Shanks, H.: Optical phonons of aluminum nitride. *J. Appl. Phys.* **55**, 4010–4014 (1984). <https://doi.org/10.1063/1.332989>
- Chaurasia, H., Tripathi, S.K., Bilgaiyan, K., Pandey, A., Mukhopadhyay, K., Agarwal, K., et al.: Preparation and properties of AlN (aluminum nitride) powder/thin films by single source precursor. *New J. Chem.* **43**, 1900–1909 (2019). <https://doi.org/10.1039/C8NJ04594A>
- Chen, H.-Y., Han, S., Shih, H.C.: The characterization of aluminum nitride thin films prepared by dual ion beam sputtering. *Surf. Coat. Technol.* **200**, 3326–3329 (2006). <https://doi.org/10.1016/j.surfcoat.2005.07.046>
- Cheng, H., Sun, Y., Zhang, J., Zhang, Y., Yuan, S., Hing, P.: AlN films deposited under various nitrogen concentrations by RF reactive sputtering. *J. Cryst. Growth* **254**, 46–54 (2003). [https://doi.org/10.1016/S0022-0248\(03\)01176-X](https://doi.org/10.1016/S0022-0248(03)01176-X)

- Choudhary, R., Mishra, P., Biswas, A., Bidaye, A.: Structural and optical properties of aluminum nitride thin films deposited by pulsed DC magnetron sputtering. *Int. Sch. Res. Not.* **2013**, 759462 (2013). <https://doi.org/10.1155/2013/759462>
- Davis, R.F.: III-V nitrides for electronic and optoelectronic applications. *Proc. IEEE* **79**, 702–712 (1991). <https://doi.org/10.1109/5.90133>
- Dogheche, E., Rémiens, D., Boudrioua, A., Loulergue, J.: Growth and optical characterization of aluminum nitride thin films deposited on silicon by radio-frequency sputtering. *Appl. Phys. Lett.* **74**, 1209–1211 (1999). <https://doi.org/10.1063/1.123501>
- Drum, C., Mitchell, J.: Electron microscopic examination of role of axial dislocations in growth of AlN whiskers. *Appl. Phys. Lett.* **4**, 164–165 (1964). <https://doi.org/10.1063/1.1754015>
- Fasasi, A.Y., Osagie, E., Pelemo, D., Obiajunwa, E., Ajenifuja, E., Ajao, J., et al.: Effect of precursor solvents on the optical properties of copper oxide thin films deposited using spray pyrolysis for optoelectronic applications. *Am. J. Mater. Synth. Process.* **3**, 12–22 (2018). <https://doi.org/10.11648/j.ajmsp.20180302.12>
- Gerlich, D., Dole, S., Slack, G.: Elastic properties of aluminum nitride. *J. Phys. Chem. Solids* **47**, 437–441 (1986). [https://doi.org/10.1016/0022-3697\(86\)90039-9](https://doi.org/10.1016/0022-3697(86)90039-9)
- Goldsmith, J.H., Vangala, S., Hendrickson, J.R., Cleary, J.W., Vella, J.H.: Long-wave infrared selective pyroelectric detector using plasmonic near-perfect absorbers and highly oriented aluminum nitride. *JOSA B* **34**, 1965–1970 (2017). <https://doi.org/10.1364/JOSAB.34.001965>
- Gooch, J.W.: Sellmeier equation. *Encycl. Dict. Polym.* (2011). [https://doi.org/10.1007/978-1-4419-6247-8\\_10447](https://doi.org/10.1007/978-1-4419-6247-8_10447)
- Gräupner, P., Pommier, J., Cachard, A., Coutaz, J.: Electro-optical effect in aluminum nitride waveguides. *J. Appl. Phys.* **71**, 4136–4139 (1992). <https://doi.org/10.1063/1.350844>
- He, X., Wen, Q., Lu, Z., Shang, Z., Wen, Z.: A micro-electromechanical systems based vibration energy harvester with aluminum nitride piezoelectric thin film deposited by pulsed direct-current magnetron sputtering. *Appl. Energy* **228**, 881–890 (2018). <https://doi.org/10.1016/j.apenergy.2018.07.001>
- Huang, C., Fan, J., Zhang, R., Zhu, L.: Internal frequency mixing in a single optomechanical resonator. *Appl. Phys. Lett.* **101**, 231112 (2012). <https://doi.org/10.1063/1.4769838>
- Interrante, L.V., Lee, W., McConnell, M., Lewis, N., Hall, E.: Preparation and properties of aluminum nitride films using an organometallic precursor. *J. Electrochem. Soc.* **136**, 472 (1989). <https://doi.org/10.1149/1.2096657>
- Kasap, S., Capper, P.: Springer handbook of electronic and photonic materials. Springer, Cham (2017)
- Khoshman, J.M., Kordesch, M.E.: Spectroscopic ellipsometry characterization of amorphous aluminum nitride and indium nitride thin films. *Physica Status Solidi (c)* **2**, 2821–2827 (2005). <https://doi.org/10.1002/pssc.200461331>
- Kuang, X.-P., Zhang, H.-Y., Wang, G.-G., Cui, L., Zhu, C., Jin, L., et al.: AlN films prepared on 6H-SiC substrates under various sputtering pressures by RF reactive magnetron sputtering. *Appl. Surf. Sci.* **263**, 62–68 (2012). <https://doi.org/10.1016/j.apsusc.2012.08.121>
- Kumar, A., Prasad, M., Janyani, V., Yadav, R.: Fabrication and simulation of piezoelectric aluminium nitride based micro electro mechanical system acoustic sensor. *J. Nanoelectron. Optoelectron.* **14**, 1267–1274 (2019). <https://doi.org/10.1166/jno.2019.2637>
- Larciprete, M.C., Bosco, A., Belardini, A., Li Voti, R., Leahu, G., Sibilia, C., et al.: Blue second harmonic generation from aluminum nitride films deposited onto silicon by sputtering technique. *J. Appl. Phys.* **100**, 023507 (2006). <https://doi.org/10.1063/1.2219151>
- Liu, Y., Cong, H., Cheng, H.: Thermal properties of nanocrystalline Al composites reinforced by AlN nanoparticles. *J. Mater. Res.* **24**, 24–31 (2009a). <https://doi.org/10.1557/JMR.2009.0034>
- Liu, Y., Cong, H., Wang, W., Sun, C., Cheng, H.: AlN nanoparticle-reinforced nanocrystalline Al matrix composites: fabrication and mechanical properties. *Mater. Sci. Eng. A* **505**, 151–156 (2009b). <https://doi.org/10.1016/j.msea.2008.12.045>
- Lu, T.-J., Fanto, M., Choi, H., Thomas, P., Steidle, J., Mouradian, S., et al.: Aluminum nitride integrated photonics platform for the ultraviolet to visible spectrum. *Opt. Express* **26**, 11147–11160 (2018). <https://doi.org/10.1364/OE.26.011147>
- Luque-Raigón, J.M., Halme, J., López-López, C.: Angular optical behavior of photonic-crystal-based dye-sensitized solar cells. *J. Photonics Energy* **9**, 025501 (2019). <https://doi.org/10.1117/1.JPE.9.025501>
- Mahmood, A., Rakov, N., Xiao, M.: Influence of deposition conditions on optical properties of aluminum nitride (AlN) thin films prepared by DC-reactive magnetron sputtering. *Mater. Lett.* **57**, 1925–1933 (2003). [https://doi.org/10.1016/S0167-577X\(02\)01106-0](https://doi.org/10.1016/S0167-577X(02)01106-0)
- Morkoc, B.H., Strite, S., Gao, G., Lin, M., Sverdlov, B., Burns, M.: Large-band-gap SiC, III-V nitride, and II-VI ZnSe-based semiconductor device technologies. *J. Appl. Phys.* **76**, 1363–1398 (1994). <https://doi.org/10.1063/1.358463>

- Nam, K., Hong, K., Park, H., Choe, H.: Facile synthesis of powder-based processing of porous aluminum nitride. *J. Eur. Ceram. Soc.* **38**, 1164–1169 (2018). <https://doi.org/10.1016/j.jeurceramsoc.2017.09.049>
- Ohira, S., Iwaki, M.: Formation of AlN by nitrogen molecule ion implantation. *Nucl. Instrum. Methods Phys. Res., Sect. B* **19**, 162–166 (1987). [https://doi.org/10.1016/S0168-583X\(87\)80034-4](https://doi.org/10.1016/S0168-583X(87)80034-4)
- Ou, K.-L., Chen, C.-C., Lin, C.-T., Chen, C.-S., Lin, C.-C., Lee, S.-Y.: Application of aluminum nitride thin film on biosensing of cell differentiation. *J. Electrochem. Soc.* **154**, P11 (2006). <https://doi.org/10.1149/1.2402992>
- Pezzagna, S., Brault, J., Leroux, M., Massies, J., De Micheli, M.: Refractive indices and elasto-optic coefficients of GaN studied by optical waveguiding. *J. Appl. Phys.* **103**, 123112 (2008). <https://doi.org/10.1063/1.2947598>
- Radwan, M., Bahgat, M.: A modified direct nitridation method for formation of nano-AlN whiskers. *J. Mater. Process. Technol.* **181**, 99–105 (2007). <https://doi.org/10.1016/j.jmatprotec.2006.03.045>
- Rensch, U., Eichhorn, G.: Investigation of the state of strain and of the electrical properties of AlN layers on monocrystalline Si. *Physica Status Solidi (a)* **90**, 135–141 (1985). <https://doi.org/10.1002/pssa.2210900111>
- Rosenberg, Z., Brar, N., Bless, S.: Dynamic high-pressure properties of AlN ceramic as determined by flyer plate impact. *J. Appl. Phys.* **70**, 167–171 (1991). <https://doi.org/10.1063/1.350337>
- Schupp, T., Lischka, K., As, D.: MBE growth of atomically smooth non-polar cubic AlN. *J. Cryst. Growth* **312**, 1500–1504 (2010). <https://doi.org/10.1016/j.jcrysgro.2010.01.040>
- Shi, Z., Yang, W., Kang, Y., Qiao, G., Jin, Z.: Synthesis of AlN porous-shell hollow spheres by a combustion route. *Ceram. Int.* **39**, 4663–4667 (2013). <https://doi.org/10.1016/j.ceramint.2012.10.235>
- Shi, X., Yu, X., Nie, C., Li, F., Zhang, S.: Controlled growth of nanocrystalline aluminum nitride films for full color range. *Ceram. Int.* **47**, 21546–21553 (2021). <https://doi.org/10.1016/j.ceramint.2021.04.166>
- Shin, W., Sun, Y., Soltani, M., Mi, Z.: Demonstration of green and UV wavelength high Q aluminum nitride on sapphire microring resonators integrated with microheaters. *Appl. Phys. Lett.* **118**, 211103 (2021). <https://doi.org/10.1063/5.0052163>
- Sinha, N., Wabiszewski, G.E., Mahameed, R., Felmetsger, V.V., Tanner, S.M., Carpick, R.W., et al.: Piezoelectric aluminum nitride nanoelectromechanical actuators. *Appl. Phys. Lett.* **95**, 053106 (2009). <https://doi.org/10.1063/1.3194148>
- Stolz, A., Soltani, A., Abdallah, B., Charrier, J., Deresmes, D., Jouan, P.-Y., et al.: Optical properties of aluminum nitride thin films grown by direct-current magnetron sputtering close to epitaxy. *Thin Solid Films* **534**, 442–445 (2013). <https://doi.org/10.1016/j.tsf.2013.01.086>
- Strite, A.S., Morkoç, H.: GaN, AlN, and InN: a review. *J. Vac. Sci. Technol. B: Microelectron. Nanometer Struct. Process., Meas., Phenom.* **10**, 1237–1266 (1992). <https://doi.org/10.1116/1.585897>
- Takikawa, H., Kimura, K., Miyano, R., Sakakibara, T., Bendavid, A., Martin, P.J., et al.: Effect of substrate bias on AlN thin film preparation in shielded reactive vacuum arc deposition. *Thin Solid Films* **386**, 276–280 (2001). [https://doi.org/10.1016/S0040-6090\(00\)01673-4](https://doi.org/10.1016/S0040-6090(00)01673-4)
- Valbin, L., Sevely, L.: Piezoelectric aluminum nitride thin films for ultrasonic transducers. *MEMS Compon. Appl. Ind., Automob., Aerosp., Commun.* **4559**, 95–102 (2001). <https://doi.org/10.1117/12.443023>
- Van Bui, H., Nguyen, M., Wiggers, F.B., Aarnink, A.A., de Jong, M.P., Kovalgin, A.Y.: Self-limiting growth and thickness-and temperature-dependence of optical constants of ALD AlN thin films. *ECS J. Solid State Sci. Technol.* **3**, P101 (2014). <https://doi.org/10.1149/2.020404jss>
- Van Bui, H., Wiggers, F.B., Gupta, A., Nguyen, M.D., Aarnink, A.A., de Jong, M.P., et al.: Initial growth, refractive index, and crystallinity of thermal and plasma-enhanced atomic layer deposition AlN films. *J. Vac. Sci. Technol. A* **33**, 01A111 (2015). <https://doi.org/10.1116/1.4898434>
- Venkataraj, S., Severin, D., Drese, R., Koerfer, F., Wuttig, M.: Structural, optical and mechanical properties of aluminium nitride films prepared by reactive DC magnetron sputtering. *Thin Solid Films* **502**, 235–239 (2006). <https://doi.org/10.1016/j.tsf.2005.07.281>
- Vispute, R., Wu, H., Narayan, J.: High quality epitaxial aluminum nitride layers on sapphire by pulsed laser deposition. *Appl. Phys. Lett.* **67**, 1549–1551 (1995). <https://doi.org/10.1063/1.114489>
- Wang, Y., Li, Y., Feng, W., Li, W., Zhao, C., Liu, L., et al.: Influence of thickness on field emission characteristics of AlN thin films. *Appl. Surf. Sci.* **243**, 394–400 (2005). <https://doi.org/10.1016/j.apsusc.2004.09.111>
- Watanabe, N., Kimoto, T., Suda, J.: The temperature dependence of the refractive indices of GaN and AlN from room temperature up to 515 °C. *J. Appl. Phys.* **104**, 106101 (2008). <https://doi.org/10.1063/1.3021148>
- Watanabe, N., Kimoto, T., Suda, J.: Determination of the thermo-optic coefficients of GaN and AlN up to 515 °C. *Phys. Status Solidi C* **6**, S776–S779 (2009). <https://doi.org/10.1002/pssc.200880937>
- Wu, Q., Hu, Z., Wang, X., Lu, Y., Huo, K., Deng, S., et al.: Extended vapor–liquid–solid growth and field emission properties of aluminium nitride nanowires. *J. Mater. Chem.* **13**, 2024–2027 (2003). <https://doi.org/10.1039/B303987K>
- Wu, Q., Hu, Z., Wang, X., Hu, Y., Tian, Y., Chen, Y.: A simple route to aligned AlN nanowires. *Diam. Relat. Mater.* **13**, 38–41 (2004). <https://doi.org/10.1016/j.diamond.2003.08.017>

- Xiong, C., Pernice, W.H., Sun, X., Schuck, C., Fong, K.Y., Tang, H.X.: Aluminum nitride as a new material for chip-scale optomechanics and nonlinear optics. *New J. Phys.* **14**, 095014 (2012). <https://doi.org/10.1088/1367-2630/14/9/095014>
- Yarar, E., Hrkac, V., Zamponi, C., Piorra, A., Kienle, L., Quandt, E.: Low temperature aluminum nitride thin films for sensory applications. *AIP Adv.* **6**, 075115 (2016). <https://doi.org/10.1063/1.4959895>
- Yoshida, S., Misawa, S., Itoh, A.: Epitaxial growth of aluminum nitride films on sapphire by reactive evaporation. *Appl. Phys. Lett.* **26**, 461–462 (1975). <https://doi.org/10.1063/1.88210>
- Yu, C., Kim, S., Meikle, S., Doan, T., Blalock, G.: Deposition, Characterization, and Application of Aluminum Nitride Thin Films for Microelectronics. *MRS Online Proc. Libr. (OPL)* **264**, 401 (1992). <https://doi.org/10.1557/PROC-264-401>
- Zaky, Z.A., Aly, A.H.: Highly sensitive salinity and temperature sensor using Tamm resonance. *Plasmonics* **16**, 2315–2325 (2021). <https://doi.org/10.1007/s11468-021-01487-6>
- Zaky, Z.A., Aly, A.H.: Novel smart window using photonic crystal for energy saving. *Sci. Rep.* **12**, 10104 (2022). <https://doi.org/10.1038/s41598-022-14196-9>
- Zaky, Z.A., Sharma, A., Alamri, S., Aly, A.H.: Theoretical evaluation of the refractive index sensing capability using the coupling of Tamm-Fano resonance in one-dimensional photonic crystals. *Appl. Nanosci.* **11**, 2261–2270 (2021a). <https://doi.org/10.1007/s13204-021-01965-7>
- Zaky, Z.A., Sharma, A., Alamri, S., Saleh, N., Aly, A.H.: Detection of fat concentration in milk using ternary photonic crystal. *SILICON* **14**, 6063–6073 (2021b). <https://doi.org/10.1007/s12633-021-01379-8>
- Zaky, Z.A., Al-Dossari, M., Matar, Z., Aly, A.H.: Effect of geometrical and physical properties of cantor structure for gas sensing applications. *Synth. Met.* **291**, 117167 (2022a). <https://doi.org/10.1016/j.synthmet.2022.117167>
- Zaky, Z.A., Amer, H.A., Suthar, B., Aly, A.H.: Gas sensing applications using magnetized cold plasma multilayers. *Opt. Quant. Electron.* **54**, 217 (2022b). <https://doi.org/10.1007/s11082-022-03594-y>
- Zaky, Z.A., Hanafy, H., Panda, A., Pukhrambam, P.D., Aly, A.H.: Design and analysis of gas sensor using tailorable fano resonance by coupling between Tamm and defected mode resonance. *Plasmonics* **17**, 2103–2111 (2022c). <https://doi.org/10.1007/s11468-022-01699-4>
- Zaky, Z.A., Singh, M.R., Aly, A.H.: Tamm resonance excited by different metals and graphene. *Photon. Nanostruct.-Fundam. Appl.* (2022d). <https://doi.org/10.1016/j.photonics.2022.100995>
- Zaky, Z.A., Mohaseb, M., Panda, A., Amer, H.A., Farag, A.M., Kovac, J., et al.: Theoretical analysis of porous silicon one-dimensional photonic crystal doped with magnetized cold plasma for hazardous gases sensing applications. *Opt. Quant. Electron.* **55**, 584 (2023a). <https://doi.org/10.1007/s11082-023-04907-5>
- Zaky, Z.A., Al-Dossari, M., Zohny, E.I., Aly, A.H.: Refractive index sensor using Fibonacci sequence of gyroidal graphene and porous silicon based on Tamm plasmon polariton. *Opt. Quant. Electron.* **55**, 6 (2023b). <https://doi.org/10.1007/s11082-022-04262-x>
- Zaky, Z.A., Al-Dossari, M., Saleh, N., Abdelhady, M.M., Sharma, A., Zhaketov, V., et al.: Photonic crystal with magnified resonant peak for biosensing applications. *Phys. Scr.* **98**, 055108 (2023c). <https://doi.org/10.1088/1402-4896/acbf1>
- Zaky, Z.A., Al-Dossari, M., Hendy, A.S., Zayed, M., Aly, A.H.: Gamma radiation detector using Cantor quasi-periodic photonic crystal based on porous silicon doped with polymer. *Int J Modern Phys B* (2024). <https://doi.org/10.1142/S0217979224504095>
- Zetterling, C.-M., Östling, M., Wongchotigul, K., Spencer, M., Tang, X., Harris, C., et al.: Investigation of aluminum nitride grown by metal–organic chemical–vapor deposition on silicon carbide. *J. Appl. Phys.* **82**, 2990–2995 (1997). <https://doi.org/10.1063/1.366136>
- Zha, X.-H., Luo, J.-T., Tao, R., Fu, C.: Surface and bulk acoustic wave resonators based on aluminum nitride for bandpass filters. *AAPPS Bull.* **34**, 14 (2024). <https://doi.org/10.1007/s43673-023-00104-4>
- Zhang, X.-L., Song, J.-F., Li, X.-B., Feng, J., Sun, H.-B.: Optical Tamm states enhanced broad-band absorption of organic solar cells. *Appl. Phys. Lett.* **101**, 243901 (2012). <https://doi.org/10.1063/1.4770316>
- Zou, Y., Gao, C., Zhou, J., Liu, Y., Xu, Q., Qu, Y., et al.: Aluminum scandium nitride thin-film bulk acoustic resonators for 5G wideband applications. *Microsyst. Nanoeng.* **8**, 124 (2022). <https://doi.org/10.1038/s41378-022-00457-0>

**Publisher's Note** Springer Nature remains neutral with regard to jurisdictional claims in published maps and institutional affiliations.

Springer Nature or its licensor (e.g. a society or other partner) holds exclusive rights to this article under a publishing agreement with the author(s) or other rightsholder(s); author self-archiving of the accepted manuscript version of this article is solely governed by the terms of such publishing agreement and applicable law.